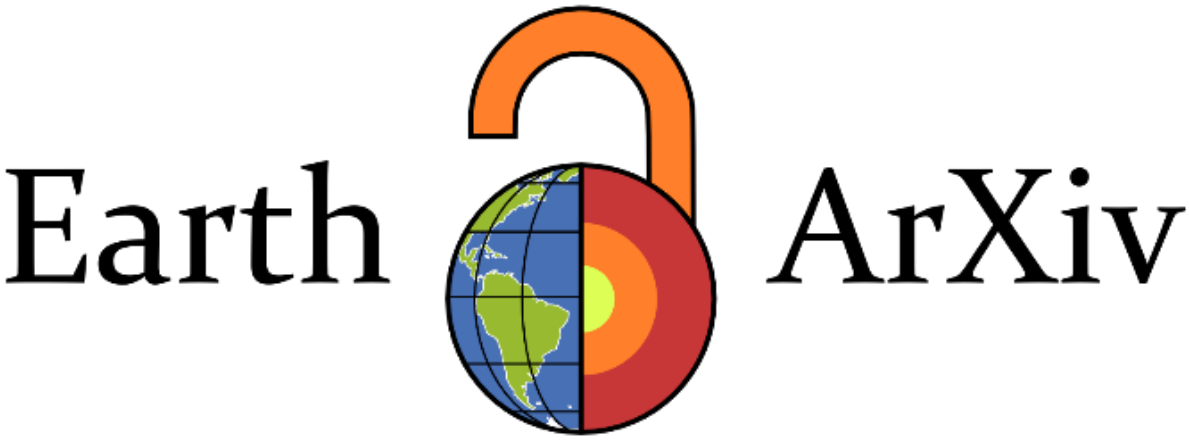

Peer review status:

This is a non-peer-reviewed preprint submitted to EarthArXiv.

Authors:

Palaash Gang: Indus International School, Pune
https://orcid.org/0009-0006-7448-9488
palaashgang@gmail.com

Aaren Bhandari: Stonehill International School, Bengaluru
aarenbhandari@gmail.com
https://orcid.org/0009-0009-7551-4122

Kianu Anggun: Jakarta Intercultural School (JIS), Jakarta
https://orcid.org/0009-0005-4629-3798
73866@jisedu.or.id

A Reproducible Framework for the Compressibility of Truncated Spherical-harmonic Planetary Potential-field Models

Palaash Gang[1*], Aaren Bhandari[2] and Kianu Anggun[3]

[1*]Indus International School, Pune, Pune, India.
[2]Stonehill International School, Bengaluru, India.
[3]Jakarta Intercultural School (JIS), Jakarta, Indonesia.

*Corresponding author(s). E-mail(s): palaashgang@gmail.com;
Contributing authors: aarenbhandari@gmail.com; 73866@jisedu.or.id;

Abstract

For a planetary potential field whose degree-variance spectrum decays as a convergent power law $\boldsymbol{\sigma_\ell^2 \sim \ell^{-\alpha}}$ $(\boldsymbol{\alpha > 1})$, a single measured exponent simultaneously fixes three classically distinct rates: the truncation-error decay rate, the Sobolev smoothness index, and the Kolmogorov $\boldsymbol{n}$-width rate. Spherical-harmonic degree truncation is the standard yet inherently lossy way to compress such fields, and this identification turns its efficiency into a direct readout of spectral character. Our contribution is empirical and information-theoretic: we measure the collapse of all three rates onto one exponent, field by field, across real gravity, geomagnetic, crustal, and planetary data (Earth, Moon, Mars), and we map where the power-law regime holds and where it breaks. The fields are synthesized via exact Gauss–Legendre quadrature and checked for implementation exactness against the Parseval identity to better than $\boldsymbol{10^{-13}}$. Compressibility tracks physical source depth: the deep, dipole-dominated core field proves intrinsically compact, the shallow crustal field remains nearly incompressible, and the geoid occupies the intermediate space. Because spherical-harmonic truncation is coefficient-optimal for these red-spectrum fields in the rate (order) sense, residual storage inefficiency stems from bit allocation rather than basis choice; we quantify it by comparing float32 storage against an independent-Gaussian rate–distortion reference and realized coders. All data, code, and figures in this work reproduce from a single pipeline command.

Keywords: Spherical harmonics, spectral truncation, geoid, geomagnetic field, degree variance, data compression

1 Introduction

How many numbers does it take to represent a planetary potential field to relative accuracy ε, and is spherical-harmonic degree truncation an efficient way to store them? These questions arise whenever a global model must be stored, transmitted, or evaluated at limited precision: choosing $\ell_{\max}$ too small sacrifices accuracy, while retaining all coefficients wastes storage on degrees that add nothing above the measurement noise. Despite the ubiquity of truncated spherical-harmonic models in geodesy and geomagnetism, the truncation-accuracy trade-off has not been placed on a common, rigorously verified, cross-field footing that also quantifies information-theoretic efficiency.

Earth's gravity field is routinely represented by truncated spherical-harmonic models such as the Earth Gravitational Model 2008 (EGM2008), which nominally reaches degree 2190 (Pavlis et al. 2012); calibrated International Center for Global Earth Models (ICGEM) commission errors put its per-degree signal-to-noise ratio (SNR) below unity at about degree 1787 (computed in the pipeline from the model's calibrated ICGEM commission errors; `results/bandlimit.csv`), the effective information ceiling beyond which the remaining degrees amplify noise rather than resolve signal. The GRACE and GOCE missions constrain its long-to-medium wavelengths (Tapley et al. 2004; Pail et al. 2011), and combined models reach an ≈9 km harmonic half-wavelength over land (Hirt et al. 2013) (the finer ∼200 m sometimes quoted is the auxiliary topographic grid spacing, not the harmonic resolution; see Appendix A). The geomagnetic main field is described by the International Geomagnetic Reference Field (IGRF), whose thirteenth generation reaches degree 13 (Alken et al. 2021; Finlay et al. 2016). Although each spectrum is well characterised individually—gravity by Kaula's power law (Kaula 1963, 1966), the main field by the Lowes–Mauersberger spectrum (Mauersberger 1956; Lowes 1966)—a common normalised compression footing and explicit information-theoretic bound have not been reported.

This paper provides a reproducible computational framework that brings approximation-theoretic and information-theoretic tools, such as spectral-decay laws, Sobolev smoothness, the Kolmogorov n-width, and rate-distortion analysis, to the information content and compression efficiency of real planetary potential fields, on a common footing spanning gravity, geomagnetic, crustal, and planetary models.

Contribution. The three approximation-theoretic ingredients used here—the spectral-decay slope law, the Sobolev summability criterion, and the Kolmogorov n-width rate for Sobolev classes on the sphere—are classical, and their joint identification under a single spectral exponent is the L^2, power-law specialisation of the standard approximation-space characterisation that ties the rate of best approximation to the order of smoothness (Proposition 1); we present it as such. What this framework contributes is threefold. First, the *measured* collapse of all three rates onto one exponent, confirmed field by field on real data—the EGM2008 geoid, the IGRF-13 radial main field B_r, and the NGDC-720 crustal field, extended to the Moon and Mars geoids, derived gravity functionals, and two IGRF epochs—with the underlying error identity checked against the Parseval relation to better than 10^{-13} throughout, and with the regime boundaries mapped: the law holds for $\alpha > 1$, the band-limited main field enters

only through effective indices, and the near-white crustal field lies outside it. Second, an information-theoretic quantification of storage efficiency, comparing float32 coefficient storage against an independent-Gaussian rate–distortion reference and against realised greedy and entropy coders on the same coefficient sets. Third, an open, tested, single-command pipeline with pinned dependencies and automated verification, from which every figure and table regenerates.

2 Theoretical Framework

A real, square-integrable function f on the unit sphere expands in 4π-normalised real spherical harmonics,

$$f(\theta,\phi) = \sum_{\ell\geq 0}\sum_{m=-\ell}^{\ell} c_{\ell m}\, Y_{\ell m}(\theta,\phi)$$

(Wieczorek and Meschede 2018), where the degree ℓ sets the spatial scale, resolving features of angular size roughly $180^\circ/\ell$. The truncation operator $S_{\ell_{\max}}$ keeps only the terms with $\ell \leq \ell_{\max}$, and we measure reconstruction quality by the area-weighted relative L^2 error

$$\varepsilon(\ell_{\max}) = \|f - S_{\ell_{\max}} f\|/\|f\|.$$

Orthonormality of the harmonics (Parseval's relation) gives

$$\|f\|^2 = 4\pi \sum_{\ell} \sigma_\ell^2, \qquad \text{with per-degree variance} \qquad \sigma_\ell^2 = \sum_m c_{\ell m}^2,$$

and because truncation removes whole degrees the error has the exact closed form

$$\varepsilon^2(\ell_{\max}) = \frac{\sum_{\ell>\ell_{\max}} \sigma_\ell^2}{\sum_\ell \sigma_\ell^2}. \tag{1}$$

Throughout we adopt the convention $\sigma_\ell^2 = \sum_m c_{\ell m}^2$, the per-degree power summed over order m.

Remark. Monotonicity of $\varepsilon(\ell_{\max})$ is automatic rather than empirical. By (1), $\varepsilon^2(\ell_{\max}) = S^{-1}\sum_{\ell>\ell_{\max}} \sigma_\ell^2$ with $S = \sum_\ell \sigma_\ell^2 > 0$ and $\sigma_\ell^2 = \sum_m c_{\ell m}^2 \geq 0$; incrementing $\ell_{\max}$ removes the single non-negative term $\sigma_{\ell_{\max}+1}^2$ from the numerator and leaves S unchanged, so $\varepsilon^2(\ell_{\max}+1) - \varepsilon^2(\ell_{\max}) = -\sigma_{\ell_{\max}+1}^2/S \leq 0$, strictly negative iff $\sigma_{\ell_{\max}+1}^2 > 0$, and $\varepsilon(\ell_{\mathrm{ref}}) = 0$ once the tail is empty. The monotone, correctly-ordered error curves reported for every field in Section 4 are therefore a structural consequence.

The recovered spectral index is convention-dependent: a per-coefficient normalisation $\sigma_\ell^2/(2\ell+1)$, or the Lowes–Mauersberger $(\ell+1)$ factor appropriate to the radial field, shifts the index by one (Backus et al. 1996; Lowes 1966; Mauersberger 1956; Maus 2008). The three results derived next are classical, as noted in the Introduction; their joint identification under one exponent is the power-law specialisation of that classical theory, and what is established below is its quantitative, cross-field measurement.

Spectral decay and the truncation-error slope. Model the tail of the degree-variance spectrum as a power law $\sigma_\ell^2 = C\,\ell^{-\alpha}$ with $\alpha > 1$, so that the total power is finite; this is the standard Kaula-type description of geophysical spectra (Kaula 1966, 1963; Rapp 1989). The discarded power is the tail sum $T(\ell_{\max}) = \sum_{\ell>\ell_{\max}} C\,\ell^{-\alpha} = C\sum_{\ell\ge\nu}\ell^{-\alpha}$ with start index $\nu = \ell_{\max}+1$ (distinct from the retained-coefficient count $N = (\ell_{\max}+1)^2$ used below). Apply the Euler–Maclaurin summation formula to $g(x) = x^{-\alpha}$ in its first-order form with exact integral remainder,

$$\sum_{\ell\ge\nu} g(\ell) = \int_\nu^\infty g(x)\,dx + \tfrac{1}{2}g(\nu) + \rho_\alpha(\nu), \qquad \rho_\alpha(\nu) = \int_\nu^\infty P_1(x)\,g'(x)\,dx,$$

where $P_1(x) = \{x\} - \frac{1}{2}$ is the first periodic Bernoulli polynomial, the mean-zero sawtooth. Evaluating $\int_\nu^\infty x^{-\alpha}\,dx = \nu^{1-\alpha}/(\alpha-1)$—finite precisely because $\alpha > 1$—together with $g(\nu) = \nu^{-\alpha}$ gives the exact identity

$$T(\ell_{\max}) = \frac{C\,\nu^{1-\alpha}}{\alpha-1} + \frac{C}{2}\,\nu^{-\alpha} + C\,\rho_\alpha(\nu). \tag{2}$$

The remainder is lower-order. Integrating ρ_α by parts once against the second periodic Bernoulli function P_2 (which satisfies $P_2' = 2P_1$, equals $\frac{1}{6}$ at the integers, and has $|P_2| \le \frac{1}{6}$) yields $\rho_\alpha(\nu) = -\frac{1}{12}g'(\nu) - \frac{1}{2}\int_\nu^\infty P_2(x)\,g''(x)\,dx$, and since $g'(x) = -\alpha x^{-\alpha-1}$ and $g''(x) = \alpha(\alpha+1)x^{-\alpha-2}$ keep a fixed sign,

$$|\rho_\alpha(\nu)| \le \tfrac{1}{12}|g'(\nu)| + \tfrac{1}{12}\int_\nu^\infty |g''(x)|\,dx = \frac{\alpha}{12}\nu^{-\alpha-1} + \frac{\alpha}{12}\nu^{-\alpha-1} = \frac{\alpha}{6}\,\nu^{-\alpha-1}. \tag{3}$$

Thus $C\,\rho_\alpha(\nu) = O(\nu^{-\alpha-1})$ with an explicit constant: the leading term $C(\alpha-1)^{-1}\nu^{1-\alpha} \sim C(\alpha-1)^{-1}\ell_{\max}^{1-\alpha}$ fixes the decay rate, the half-boundary term is the first correction, and (3) bounds everything beyond it. The hypothesis $\alpha > 1$ is exactly the condition that the improper integral, and hence the total power $S = \sum_\ell \sigma_\ell^2$, converge; when it fails (the near-white crustal spectrum below) the expansion, and with it the slope law, no longer applies. Combining this with (1) yields

$$\varepsilon(\ell_{\max}) \sim K\,\ell_{\max}^{(1-\alpha)/2}, \qquad K = \sqrt{\frac{C}{S(\alpha-1)}}, \quad S = \sum_\ell \sigma_\ell^2, \tag{4}$$

so the log–log slope is $p = (1-\alpha)/2$, equivalently $\alpha = 1 - 2p$. This is the large-$\ell_{\max}$ *asymptotic* slope; a slope fitted over a finite degree window is a tail-weighted average and can differ slightly from $(1-\alpha)/2$ even for a pure power law. As a numeric corollary, the measured geoid slope -0.861 implies $\alpha = 1 - 2p \approx 2.72$, whereas a direct weighted fit of the degree-variance spectrum gives $\alpha = 2.839$; the roughly 4% gap reflects the geoid's mild departure from a single power law, since Kaula's rule is only approximate (Rapp 1989). The remainder bound (3) certifies the $O(\nu^{-\alpha-1})$ decay analytically; numerically, for the idealised power law itself, retaining the Bernoulli corrections reproduces its exact tail sum to better than 10^{-9} at $\ell_{\max} = 100$.

Sobolev regularity of the field. The natural smoothness scale is the Sobolev space $H^s(S^2)$ defined through the Laplace–Beltrami operator, whose eigenvalue on degree ℓ is $\ell(\ell+1)$: one has $f \in H^s(S^2)$ if and only if

$$\|f\|_{H^s}^2 = \sum_{\ell} \big(1+\ell(\ell+1)\big)^s \sigma_\ell^2 < \infty$$

(Atkinson and Han 2012; Dai and Xu 2013), where the H^s norm is normalised without the 4π solid-angle factor, so that $\|f\|_{H^0}^2 = \sum_\ell \sigma_\ell^2 = \|f\|_{L^2}^2/4\pi$. With the large-degree weight $\big(1+\ell(\ell+1)\big)^s \sim \ell^{2s}$ and the power-law spectrum $\sigma_\ell^2 \sim \ell^{-\alpha}$, the summand of the H^s norm behaves as

$$\big(1+\ell(\ell+1)\big)^s \sigma_\ell^2 \sim \ell^{\,2s-\alpha},$$

which is summable exactly when this exponent falls below -1,

$$2s-\alpha < -1 \qquad \Longleftrightarrow \qquad s < \frac{\alpha-1}{2},$$

that is for every $s < s_*$ with the critical index

$$s_* = \frac{\alpha-1}{2} = -p. \tag{5}$$

Membership holds for every $s < s_*$, and s_* is the supremum rather than an attained value. The Sobolev embedding theorem on the two-dimensional sphere ($n = 2$) states that

$$H^s(S^2) \hookrightarrow C^k(S^2) \qquad \text{whenever} \qquad s > k + \tfrac{n}{2} = k+1,$$

(Atkinson and Han 2012) so a field of critical index s_* has a representative in C^k for every $k < s_* - 1$; the index therefore controls the pointwise smoothness of the discarded residual, not only its L^2 decay rate. This places the geoid in an informative borderline position. Its critical index $s_* \approx 0.9$ lies just below $s = 1$, the threshold at which the $k = 0$ embedding would certify a bounded continuous representative, so the geoid sits at the very edge of the Sobolev continuity scale: its power only just fails, in the summability sense of (5), to accumulate into a residual that this *sufficient* criterion certifies continuous. This concerns the idealised power-law model; the band-limited geoid is a smooth trigonometric polynomial at any finite truncation. That borderline regularity is the smoothness-space signature of the slow error decay measured below. The truncation decay rate and the Sobolev smoothness index are therefore the same quantity, up to estimator scatter between the slope-based and spectrum-based estimates: for the geoid $s_* \approx 0.9$ (0.86 from $-p$, 0.92 from $\alpha = 2.839$).

Remark (Kaula's rule sits at the C^0 threshold). Kaula's rule $\alpha = 3$ gives $s_* = (\alpha - 1)/2 = 1$, the borderline of the Sobolev embedding $H^s(S^2) \hookrightarrow C^0(S^2)$ ($s > 1$); the measured geoid index $\alpha = 2.839$ ($s_* \approx 0.92$) therefore places the real geoid marginally on the rough side of Kaula's own threshold, in the idealised infinite-band sense above.

Coefficient optimality (Kolmogorov n-width). For the Sobolev unit ball $B^s = \{ f : \|f\|_{H^s(S^2)} \le 1 \}$, classical n-width theory gives the L^2 Kolmogorov n-width

$$d_n(B^s, L^2) = \inf_{\dim V_n = n} \sup_{f \in B^s} \inf_{g \in V_n} \|f - g\|_{L^2}, \tag{6}$$

which for the two-dimensional sphere decays as $d_n \sim n^{-s/2}$ (Pinkus 1985; Kamzolov 1982). The harmonic subspace $\Pi_L = \mathrm{span}\{Y_{\ell m} : \ell \le L\}$ of dimension $n = (L+1)^2$ attains this rate, and the upper (attainability) direction follows directly from the same degree-variance machinery used above. For any $f \in B^s$, Parseval and the norm identity $\|f\|_{L^2}^2 = 4\pi \sum_\ell \sigma_\ell^2$ give

$$\|f - S_L f\|_{L^2}^2 = 4\pi \sum_{\ell > L} \sigma_\ell^2 = 4\pi \sum_{\ell > L} \frac{\big(1 + \ell(\ell+1)\big)^s \sigma_\ell^2}{\big(1 + \ell(\ell+1)\big)^s} \le 4\pi \big(1 + L(L+1)\big)^{-s} \|f\|_{H^s}^2, \tag{7}$$

since the weight $\big(1 + \ell(\ell+1)\big)^{-s}$ is decreasing in ℓ and hence bounded on the tail $\ell > L$ by its value $\big(1 + L(L+1)\big)^{-s}$ at $\ell = L$, while $\sum_{\ell > L} \big(1 + \ell(\ell+1)\big)^s \sigma_\ell^2 \le \|f\|_{H^s}^2$. Taking the supremum over B^s (on which $\|f\|_{H^s} \le 1$) gives

$$\sup_{f \in B^s} \|f - S_L f\|_{L^2} \le \sqrt{4\pi} \big(1 + L(L+1)\big)^{-s/2} \sim L^{-s} = n^{-s/2},$$

so Π_L realises the n-width rate. That no n-dimensional linear subspace can do asymptotically better—the matching lower bound $d_n(B^s, L^2) \gtrsim n^{-s/2}$—is the classical width estimate for Sobolev ellipsoids, which we take from (Pinkus 1985; Kamzolov 1982) rather than reprove. Hence, for the isotropic Sobolev class, spherical-harmonic degree truncation is rate-optimal among all n-dimensional linear approximations (coefficient-efficiency $\eta_{\mathrm{coeff}} = 1$ in the order sense); this is a worst-case statement over the isotropic ball, and localised or anisotropic signals can do better in other bases. The result is consistent with the slope law: with $n = (L+1)^2$ one has $\varepsilon \sim L^{-s_*} = n^{-s_*/2}$, so the error-versus-coefficient-count curve tracks the n-width at $s = s_*$.[1]

One exponent for three rates. The slope law, the Sobolev criterion, and the n-width rate were each derived above as a separate map from the spectral index α. Collecting those closed forms shows that they are not three facts but one. This coincidence is the L^2, power-law specialisation of the classical characterisation of approximation spaces, in which the rate of best approximation and the order of smoothness determine each other (DeVore and Lorentz 1993), specialised to the sphere in (Dai and Xu 2013, §4.4–4.5); Proposition 1 records that specialisation in the form the measurements below use. Function-space treatments of the geopotential are themselves established—least-squares collocation builds a reproducing-kernel space for the disturbing potential from its degree variances (Chang and Bian 2023), and the Freeden school works in degree-weighted Sobolev spaces (Freeden et al. 1998)—but treat the smoothness index

[1] The Cramér–Rao bound is a different object: it limits the variance of an unbiased estimator from noisy data through the Fisher information, whereas the present statement is a deterministic, noise-free best-approximation result, with coefficient noise treated separately.

as a stochastic or modelling choice; what is new here is its deterministic, measured instantiation across gravity, geomagnetic, and planetary fields.

Proposition 1 (Exponent unification)**.** *Let a field have a convergent power-law degree-variance tail $\sigma_\ell^2 = C\,\ell^{-\alpha}$ with $\alpha > 1$. Then the truncation-error log–log slope p, the Sobolev critical index s_*, and the field's best-approximation (approximation-number) decay exponent w—the exponent of $\ell_{\max}$ in $a_{\ell_{\max}}(f) = \inf_{g\in\Pi_{\ell_{\max}}} \|f - g\|_{L^2}$—coincide up to sign,*

$$p = -s_* = w = \frac{1-\alpha}{2},$$

and this common rate is the Kolmogorov n-width rate of the Sobolev ball B^{s_*}, which degree truncation attains. A single measured spectral exponent thus fixes all three rates at once.

Proof The three maps $\alpha \mapsto p$, $\alpha \mapsto s_*$, $\alpha \mapsto w$ were established individually above; we substitute their closed forms and compare. The slope law (4) gives the truncation-error exponent

$$p = \frac{1-\alpha}{2}.$$

The Sobolev summability criterion (5) gives the critical smoothness index

$$s_* = \frac{\alpha-1}{2}.$$

For the field itself, the best degree-$\ell_{\max}$ approximation in L^2 is degree truncation (orthogonal projection onto $\Pi_{\ell_{\max}}$), so its approximation numbers are $a_{\ell_{\max}}(f) = \|f - S_{\ell_{\max}} f\|_{L^2}$ and decay as $\ell_{\max}^{-s_*}$ by the slope law (4) with $p = -s_*$; hence the best-approximation exponent is

$$w = -s_* = -\frac{\alpha-1}{2}.$$

This rate coincides with the Kolmogorov n-width of the ball B^{s_*}: the field lies in B^s for every $s < s_*$, and (7) gives $d_n \sim n^{-s/2} \sim \ell_{\max}^{-s}$, so degree truncation attains the n-width at the critical smoothness $s = s_*$ as a boundary exponent (rather than by substituting s_* into (7), where $\|f\|_{H^{s_*}}$ need not be finite). Comparing the three right-hand sides,

$$p = \frac{1-\alpha}{2} = -\frac{\alpha-1}{2} = -s_* = w,$$

which is the stated identity. Each equality is an algebraic substitution of a previously derived closed form; the content is that three approximation-theoretic rates, defined through unrelated constructions, collapse onto the single number $(1-\alpha)/2$. □

Corollary 1 (Storage-curve realisation)**.** *Writing the retained-coefficient count as $N = (\ell_{\max}+1)^2$, the error-versus-storage curve of the same field decays as*

$$\varepsilon(N) \sim K'\,N^{-s_*/2}, \qquad K' = K,$$

with K the slope-law constant of (4), so the storage curve realises the Kolmogorov n-width rate at $s = s_*$.

Proof The slope law (4) together with $p = -s_*$ from Proposition 1 gives

$$\varepsilon \sim K\,\ell_{\max}^{p} = K\,\ell_{\max}^{-s_*}.$$

Inverting the count relation gives $\ell_{\max} = N^{1/2} - 1 \sim N^{1/2}$, hence

$$\varepsilon(N) \sim K\left(N^{1/2}\right)^{-s_*} = K\,N^{-s_*/2},$$

so $K' = K$ to leading order and $\varepsilon(N) \sim d_n$ with $n = N$ in (7). The measured storage curve of Figure 5 therefore has a stated mathematical backbone: its asymptotic log–log slope against coefficient count is $-s_*/2$, exactly half its slope against degree. □

Corollary 2 (Meissl order shift)**.** *Let Λ be a spherical multiplier operator whose symbol is asymptotically a power, $\lambda_\ell = \ell^t\big(1 + O(\ell^{-1})\big)$, as realised by the Meissl transfers of physical geodesy—the operators taking the disturbing potential to the geoid ($t = 0$), to the gravity disturbance and free-air anomaly ($t = 1$), and to the radial–radial gradient ($t = 2$) (Rummel and van Gelderen 1995). Acting on a field with convergent power-law tail $\sigma_\ell^2 \sim C\ell^{-\alpha}$, it produces degree variance $\lambda_\ell^2\sigma_\ell^2 \sim C\ell^{-(\alpha-2t)}$, so the* asymptotic *spectral index shifts*

$$\alpha \;\longmapsto\; \alpha - 2t.$$

When $\alpha - 2t > 1$, so the image remains in the convergent regime of Proposition 1, the three coupled rates shift in lockstep,

$$p \mapsto p + t, \qquad s_* \mapsto s_* - t, \qquad w \mapsto w + t,$$

and the unification identity $p = -s_* = w$ is preserved—the whole triple translates rigidly by t. If $\alpha - 2t \le 1$ the image leaves the regime and the rate identity lapses, though the index shift $\alpha \mapsto \alpha - 2t$ persists.

Proof The rescaling $\sigma_\ell^2(\Lambda f) = \lambda_\ell^2\sigma_\ell^2(f) \sim \ell^{2t}\cdot C\ell^{-\alpha} = C\ell^{-(\alpha-2t)}$ gives the asymptotic image index $\alpha' = \alpha - 2t$ (the $O(\ell^{-1})$ part of λ_ℓ leaves the leading exponent unchanged). For $\alpha' > 1$, substituting α' into the closed forms of Proposition 1 gives $p' = (1-\alpha')/2 = p + t$, $s'_* = (\alpha' - 1)/2 = s_* - t$, and $w' = -s'_* = w + t$; hence $p' = -s'_* = w'$, a rigid translation of the unified triple. □

Best-N-term approximation. In an orthonormal basis the best N-term L^2 approximation keeps the N coefficients of largest magnitude, the diagonal case of the Eckart–Young/Mirsky low-rank approximation theorem (Eckart and Young 1936; Mirsky 1960).

Lemma 1 (Best-N-term equivalence)**.** *Model the $2\ell + 1$ coefficients of degree ℓ as carrying equal power $p_\ell := \sigma_\ell^2/(2\ell+1)$. If p_ℓ is non-increasing in ℓ, then for $N = (L+1)^2$ the best N-term approximation coincides with degree truncation at $\ell_{\max} = L$.*

Proof Best N-term maximises the retained power $\sum_{(\ell,m)\in\mathcal{S}} c_{\ell m}^2$ over index sets $\mathcal{S}$ of size N; by the elementary rearrangement fact that a sum of N elements drawn from a fixed multiset is

largest when the N largest elements are taken, an optimal $\mathcal{S}$ collects the N largest coefficient powers. Under the equal-within-degree model the multiset of powers, sorted non-increasingly, lists $2 \cdot 0 + 1$ copies of p_0, then $2 \cdot 1 + 1$ copies of p_1, and so on; since p_ℓ is non-increasing, this sorted order *is* the degree order. Because

$$\sum_{\ell=0}^{L} (2\ell + 1) = (L + 1)^2 = N,$$

the N largest powers are exactly the coefficients of degrees $0, \ldots, L$, i.e. degree truncation at $\ell_{\max} = L$. □

For $\sigma_\ell^2 \sim \ell^{-\alpha}$ the per-coefficient power scales as $p_\ell \sim \ell^{-\alpha-1}$, non-increasing for all $\alpha > -1$ and hence for every field considered here, so spherical-harmonic degree truncation is essentially best-N-term globally. The hypothesis is the equal-within-degree (order-exchangeable) power model; real coefficients vary within a degree, so the coincidence is exact only in that model, and the residual—the small empirical gap of 0.3 percentage points for the geoid 1 per cent error (Table 1) between oracle best-N-term selection and straight degree truncation—is dominated by that within-degree variation, the degree-averaged powers p_ℓ being essentially monotone for a red spectrum.

Finite-band caveat for the main field. The slope law (4) is asymptotic. The IGRF-13 main field spans only $\ell = 1, \ldots, 13$, with about 93.8% of the radial-field power (degree-variance convention, epoch 2020.0) in the $\ell = 1$ dipole (Alken et al. 2021; Backus et al. 1996), so its empirical slope -2.924 is not an asymptotic exponent. A pure degree-variance spectrum $\sigma_\ell^2 \propto \ell^{-6.85}$ (the nominal slope-implied index $\alpha = 1 - 2p$), evaluated by exact Parseval over $\ell = 1, \ldots, 13$ and fitted over the same $\ell = 1$–12 window used for the main field, yields a log–log error slope of only -2.56, not -2.924; the steeper measured value reflects dipole dominance within a 13-degree band. Accordingly the main-field index $\alpha = 7.509$ and $s_* \approx 2.9$ are effective indices only, and -2.924 is best read as a dipole-dominated summary statistic.

Kaula departure and the crustal field. Under the per-degree convention, Kaula's rule corresponds to $\alpha = 3$ (slope $p = -1$); the observed geoid slope -0.861 is mildly shallower, consistent with the decay measured by Rapp (Rapp 1989). The crustal field falls outside this framework: its measured slope -0.248 would imply $\alpha \approx 1.5$, but a direct spectral fit gives $\alpha = -0.455$, and the two diverge sharply because the lithospheric spectrum is nearly white and band-limited (Maus 2008, 2010). For this field we report the measured decay slope alone and assign no spectral index α and no Sobolev index.

3 Methods

Figure 1 summarises the reproducible pipeline used throughout; the steps are detailed below.

Data and software. All coefficients were obtained through the built-in datasets of `pyshtools` version 4.14.1 (Wieczorek and Meschede 2018), accessed in June 2026. The gravity model is EGM2008 (Pavlis et al. 2012), served from the International Centre for Global Earth Models; the geomagnetic main field is IGRF-13 at epoch 2020.0 (Alken et al. 2021), served from NOAA's National Centers for Environmental Information;

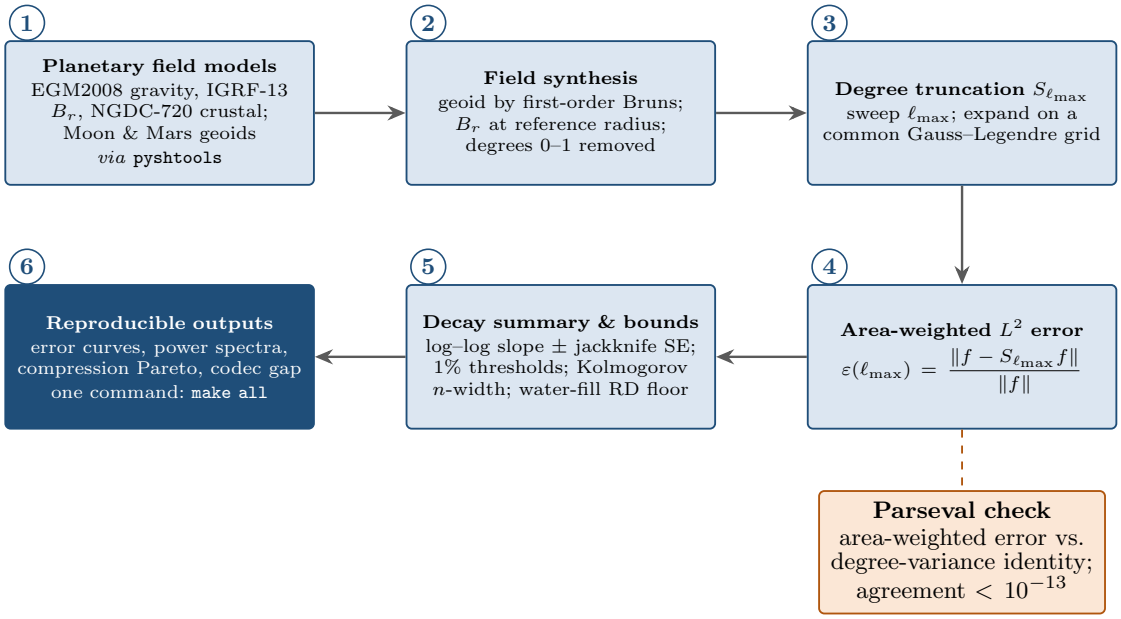

Fig. 1 Reproducible pipeline for quantifying spherical-harmonic compressibility. Planetary field models are synthesised on a Gauss–Legendre quadrature grid (stages 1–2), truncated at each degree $\ell_{\max}$ (stage 3), and compared with their reference expansion through the area-weighted relative L^2 error $\varepsilon(\ell_{\max})$ (stage 4). The error is cross-checked against the analytic Parseval degree-variance identity, and its decay is summarised by a log–log slope with a delete-one-degree jackknife sensitivity, alongside the Kolmogorov n-width and reverse water-filling bounds (stage 5); every figure and table regenerates from a single command (stage 6).

and a secondary lithospheric model, NGDC-720 (Maus 2010), is taken from the same source. The reference ellipsoid used for the geoid is WGS84 (World Geodetic System 1984), supplied by the `boule` package (Uieda and Soler 2020), with normal-field zonal coefficients following the Geodetic Reference System 1980 (Moritz 1980). Numerical work used NumPy (Harris et al. 2020) and SciPy (Virtanen et al. 2020); figures used Matplotlib (Hunter 2007) with a colour-blind-friendly palette (Wong 2011) and a diverging colour scale centred at zero for all anomaly and residual maps.

Derived scalar fields. The geoid undulation was synthesised with first-order Bruns from EGM2008 in its tide-free form, relative to the WGS84 normal field; the zero-degree term and the degree-1 geocentre term were removed, so no constant offset or geocentre shift enters the analysed undulation, and the residual degree-2 term, which after ellipsoid removal is an anomaly rather than the bulk flattening, was retained. The radial field B_r was synthesised from IGRF-13 at the model reference radius (6371.2 km), retaining all degrees 1 through 13. The truncation error for the magnetic

field is computed from the degree variance of this B_r field itself,

$$\sigma_\ell^2(B_r) = \frac{(\ell+1)^2}{2\ell+1} \sum_m \left[(g_\ell^m)^2 + (h_\ell^m)^2\right],$$

and not from the Gauss-coefficient power directly; the conventional Lowes–Mauersberger spectrum is a rescaling of that same power, shown only for the spectral figure. The secondary crustal field was synthesised as B_r from NGDC-720, which is zero below degree 16 by construction. High-degree fields were evaluated using a stable recursion for the normalised associated Legendre functions (Holmes and Featherstone 2002). Each field was expressed as a band-limited set of coefficients normalised to 4π, so that truncating the scalar field is identical to truncating the source model.

Reference expansions and the error curve. The reference ("ground truth") for each field is its expansion to a reference degree ℓ_{ref}: 360 for the geoid, 13 for the magnetic main field, and 133 for the crustal field. For a grid of truncation degrees $\ell_{\max}$, the field was truncated, expanded onto a common grid, and compared with the reference using the relative L^2 error $\varepsilon = \|f - S_{\ell_{\max}} f\| / \|f\|$; by construction $\varepsilon(\ell_{\mathrm{ref}}) = 0$.

Exact area weighting. The error integral was evaluated on a Gauss–Legendre quadrature grid, which integrates band-limited functions exactly (Driscoll and Healy 1994; Sneeuw 1994).

Lemma 2 (Exact quadrature)**.** *Let f, g be real functions band-limited to degree L. Their area integral $\int_{S^2} f\, g\, d\Omega$ is computed without discretisation error by a product rule using at least $L+1$ Gauss–Legendre nodes in $\cos\theta$ and at least $2L+1$ equiangular nodes in ϕ.*

Proof (standard) Write the integral in (t, ϕ) with $t = \cos\theta$, so that $d\Omega = dt\, d\phi$. The products $Y_{\ell m} Y_{\ell' m'}$ $(\ell, \ell' \le L)$ carry azimuthal factors of frequency $|k| \le |m| + |m'| \le 2L$; the equiangular trapezoidal rule with $\ge 2L+1$ nodes integrates every such factor exactly and, in particular, annihilates exactly the cross-order terms $m \ne m'$, whose ϕ-integral vanishes. Only the same-order terms $m = m'$ survive, and these are genuine polynomials in t of degree $\le 2L$: for odd m the two factors $(1-t^2)^{m/2}$ combine into the polynomial $(1-t^2)^m$, giving total degree $\ell + \ell' \le 2L$. Gauss–Legendre quadrature is exact for polynomials of degree $\le 2n-1$, so $n \ge L+1$ nodes integrate them exactly (Driscoll and Healy 1994; Sneeuw 1994). The tensor-product rule therefore evaluates $\int_{S^2} f\, g\, d\Omega$ exactly. □

Applied with $f - S_{\ell_{\max}} f$ and f, both band-limited to ℓ_{ref}, Lemma 2 shows the numerator and denominator of $\varepsilon^2(\ell_{\max})$ in (1) are evaluated without quadrature error, so the grid-based ε is exact—consistent with its 10^{-13} agreement with the analytic Parseval ratio (Section 4). The area weight of grid cell (i, j) is $W_{ij} = w_i\,(2\pi/n_\phi)$, where w_i are the Gauss–Legendre latitude weights and n_ϕ is the number of longitudes; these weights sum to 4π, and the duplicated 360° meridian is excluded so that no cell is double-counted. The gravity grid has bandwidth 360; the magnetic grids are oversampled (bandwidth 90 and 133) for additional cells.

Uncertainty, fitting and thresholds. The reconstruction error is the exact area-weighted Parseval ratio and carries no sampling uncertainty, so the analysis is fully deterministic. The decay was summarised by an ordinary-least-squares fit of $\log_{10}\varepsilon$ against $\log_{10}\ell_{\max}$ over an intermediate range that avoids the low-degree head and the roll-off near ℓ_{ref} (degrees 4–300 for gravity, 1–12 for the magnetic main field, 16–110 for the crustal field), following the established practice of modelling spectral decay as a power law (Rapp 1989). The uncertainty on the slope is a delete-one-degree jackknife standard error. Because the error curve is deterministic, this is a deterministic influence diagnostic: the sensitivity of the fitted slope p to omitting any single degree, equivalently the field's departure from a single power law, weighted toward the high-leverage degrees at the ends of the fit window. A field obeying a pure power law would return a vanishing jackknife SE, so the wide main-field interval reflects its short, dipole-dominated band rather than any measurement uncertainty. We read it as a deterministic sensitivity band, not a calibrated confidence interval—the degrees form a fixed, ordered design, not the i.i.d. sample the classical jackknife assumes.

As an independent characterisation we also fit the degree-variance spectrum $\sigma_\ell^2 \propto \ell^{-\alpha}$ by weighted least squares (weights $(2\ell+1)/2$, the Kaula inverse variances of $\ln\sigma_\ell^2$), reporting α with the misfit-scaled standard error; the asymptotic relation $p = (1-\alpha)/2$ recovers the measured geoid slope but is only an effective index for the band-limited magnetic field and does not apply to the near-white crustal spectrum. The degrees at which ε crosses 15, 10, 5, 2.5 and 1 per cent were located by log–log interpolation.

Verification. Two independent checks were applied. First, the grid-based error was compared with the analytic Parseval prediction of (1). Second, an independent script recomputed the degree variances directly from the raw Gauss and Stokes coefficients—for the magnetic field using the $(\ell+1)^2/(2\ell+1)$ relation between the radial-field and Gauss-coefficient power, and for the geoid using the disturbing-potential coefficients with the ellipsoidal normal field removed—and an independent equiangular grid with explicit $\sin\theta$ weights reproduced the same error. The pipeline is driven by a single command and re-downloads nothing after the first run, so the results are reproducible.

4 Results

Reconstructed fields. Figure 2 shows the EGM2008 geoid reconstructed at four truncation degrees. At $\ell_{\max} = 10$ only continental-scale undulations are present; successively higher degrees add progressively finer structure, and the field spans roughly -113 to $+101$ m once expressed relative to the ellipsoid.

Power spectra. Figure 3 shows the degree-variance spectra. The geoid spectrum decreases slowly with degree, approximately following Kaula's rule (Kaula 1966; Rapp 1989), so a large fraction of the signal resides at high degree. The IGRF-13 Lowes–Mauersberger spectrum is dominated by the degree-1 dipole and falls steeply to the model limit at degree 13. These shapes anticipate the contrasting error decay below.

Truncation error. Figure 4 presents the relative error $\varepsilon(\ell_{\max})$ for the geoid and the radial main field with log–log fits; the error is the exact Parseval ratio, so the curves

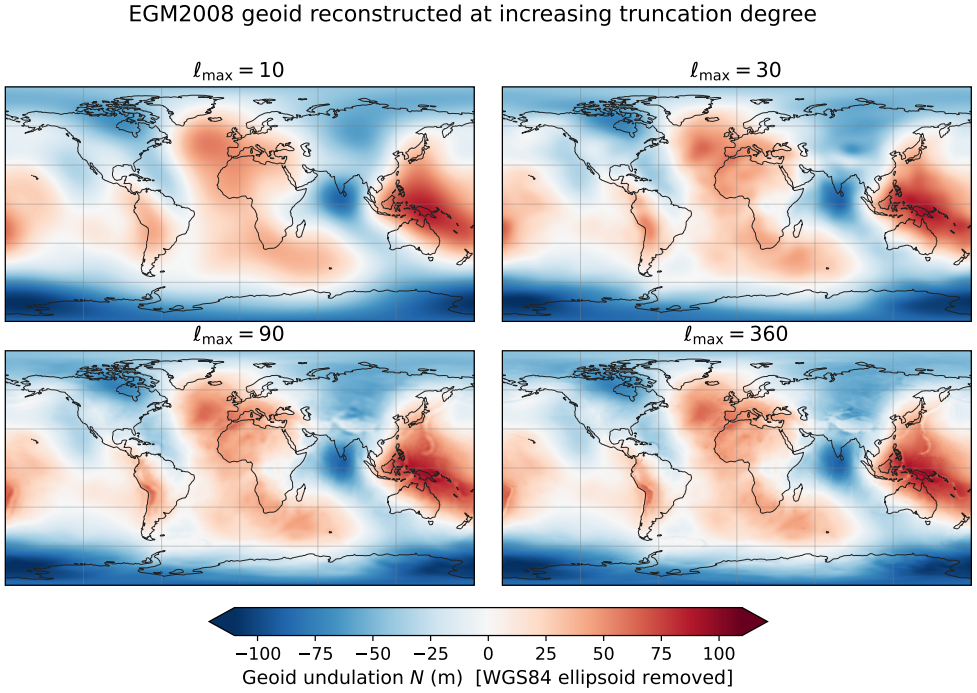

Fig. 2 EGM2008 geoid undulation N (metres, relative to WGS84) at four truncation degrees $\ell_{\max} \in \{10, 30, 90, 360\}$; degrees 0 and 1 are removed. At $\ell_{\max} = 10$ only continental-scale ($\approx$ 2000 km half-wavelength) undulations are present; each successive level adds finer structure. That appreciable power persists to $\ell_{\max} = 360$ is precisely why the error curve in Figure 4 decays slowly.

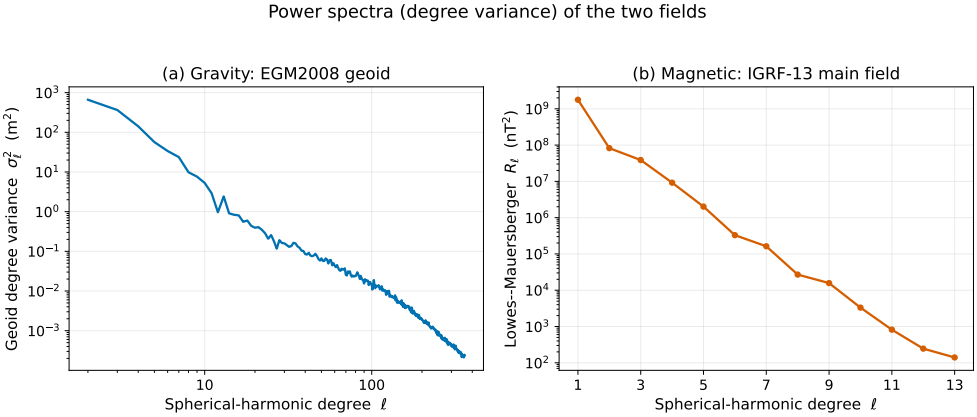

Fig. 3 Degree-variance power spectra on log–log axes. (a) EGM2008 geoid degree variance (m^2): slowly declining, with the Kaula power-law decay shown for reference. (b) IGRF-13 Lowes–Mauersberger spectrum R_ℓ (nT^2): the $\ell = 1$ dipole holds about 93.8 per cent of the radial-field power at epoch 2020.0 and the spectrum drops steeply to degree 13. The contrast in spectral slope between (a) and (b) foreshadows the contrast in error-curve decay and coefficient count quantified in Table 1.

Table 1 Headline numbers (deterministic; independently audited). The decay exponent is the log–log slope of ε against $\ell_{\max}$ with a delete-one-degree jackknife sensitivity (see Section 3); the threshold columns give the degrees at which ε crosses 10, 5 and 1 per cent, and the last column the retained-coefficient count at 1 per cent, $(\lceil \ell_{1\%} \rceil + 1)^2$, i.e. the coefficients kept when the fractional 1 per cent degree is rounded up to the next whole degree.

Field (reference degree)	Decay slope ± sensitivity	ε=10%	ε=5%	ε=1%	Coeffs at 1%
Gravity geoid (ℓ_{ref}=360)	-0.861 ± 0.033	12.1	37.5	191.2	∼37,249
Magnetic B_r (ℓ_{ref}=13)	-2.924 ± 0.724	2.5	3.4	5.9	49
Crustal B_r (ℓ_{ref}=133, sec.)	-0.248 ± 0.037	129.5	131.2	132.6	∼17,956

are deterministic and the uncertainty is carried by the fitted slope. Table 1 collects the headline numbers. For the geoid the fitted log–log slope is -0.861 ± 0.033 (jackknife sensitivity; see §3; $R^2 = 0.969$ over degrees 4–300). The error reaches 10 per cent near degree 12.1, 5 per cent near degree 37.5, 2.5 per cent near degree 94.4, and 1 per cent near degree 191.2; at degree 100 the error is 2.4 per cent, so the field is not within 1 per cent near degree 100. For the radial main field the slope is -2.924 ± 0.724 ($R^2 = 0.908$ over degrees 1–12); the large jackknife sensitivity reflects the 13-degree band, and refitting over degrees 2–12 — which drops the dipole-dominated $\ell = 1$ point — steepens the slope to about -3.65, so this exponent is best read as a dipole-dominated summary statistic rather than an asymptotic index. The error reaches 10, 5 and 1 per cent near degrees 2.5, 3.4 and 5.9, respectively. The secondary crustal field has a much shallower slope of -0.248 ± 0.037; its error remains above 10 per cent until near degree 129.5, i.e., it decays more slowly than the geoid. As an independent characterisation, a weighted fit of each degree-variance spectrum gives spectral indices $\alpha = 2.839 \pm 0.027$ (geoid), 7.509 ± 0.647 (main field) and -0.455 ± 0.042 (crustal); these are misfit-scaled fit uncertainties, not sampling confidence intervals. The asymptotic relation $p = (1 - \alpha)/2$ reproduces the geoid slope, but for the 13-degree main field it is only an effective index, and for the near-white crustal spectrum ($\alpha < 1$) it does not apply.

Storage trade-off. Figure 5 recasts the error against the number of retained coefficients $N = (\ell_{\max} + 1)^2$. Reaching 1 per cent error requires about 49 coefficients for the radial main field but about 37,249 for the geoid—a ∼760-fold difference that reflects the main field's 3.4-times steeper decay slope; the main-field curve lies below the geoid curve at every storage budget up to its degree-13 limit. The crustal curve sits near the top, requiring almost all of its coefficients to fall below 10 per cent.

Spatial pattern of the discarded signal. Figure 6 maps the geoid residual at $\ell_{\max} = 38$, the degree where the error is about 5 per cent. The discarded short-wavelength power is organised along tectonically active plate boundaries—subduction zones and trenches such as those of the Andes, Indonesia and the western Pacific, and active orogens such as the Himalaya—where short-wavelength geoid anomalies are largest (Hirt et al. 2013) because the supporting masses are only partially isostatically compensated. This spatial association is reported qualitatively, but

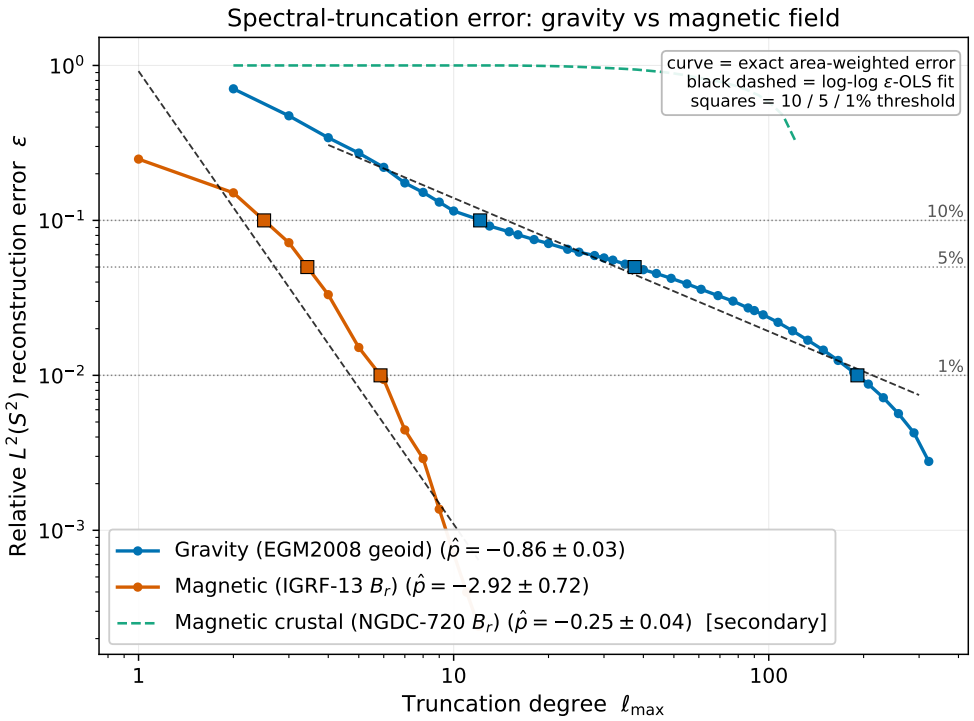

Fig. 4 Relative L^2 reconstruction error $\varepsilon(\ell_{\max})$ on log–log axes. The error is the exact area-weighted Parseval ratio; each curve is deterministic. Dashed lines show the log–log fits; squares mark the 10, 5, and 1 per cent crossings. The geoid (-0.861) and main-field (-2.924) slopes set the contrasting 1 per cent coefficient counts collected in Table 1; the crustal field (secondary) decays most slowly.

the localisation it reflects is quantitative: computed on the exact quadrature grid (`results/residual_concentration.json`), 50 per cent of the discarded energy falls in the densest 2.9 per cent of the sphere's area and 90 per cent in the densest 24.5 per cent (the densest tenth of the area alone carries 74 per cent). This concentration is the anisotropy that lets a region-adapted basis improve on the global expansion for *this* field: a basis focused on the high-residual band could capture the bulk of the discarded energy from a small area. The same concentration bounds the gain—recovering 90 per cent of the residual energy still requires resolving about a quarter of the sphere at the residual's full bandwidth—so an adapted basis improves the constant, not the n-width rate, consistent with the worst-case isotropic coefficient-optimality of §2 and the measured 0.3-point best-N-term gap.

Planetary geoids. Figure 7 plots the exact error curves for Earth, Moon and Mars.

Cross-field summary. Table 2 collects the compressibility summaries across the planetary geoids (Earth, Moon, Mars), the four Earth gravity functionals on the raw-Stokes disturbing-potential path, and two temporal epochs of the IGRF-13 main field, reporting for each the decay exponent $\hat{p}$, the spectral index $\hat{\alpha}$, the analytic asymptotic prediction $(1 - \hat{\alpha})/2$, and the 1 per cent truncation degree and coefficient count.

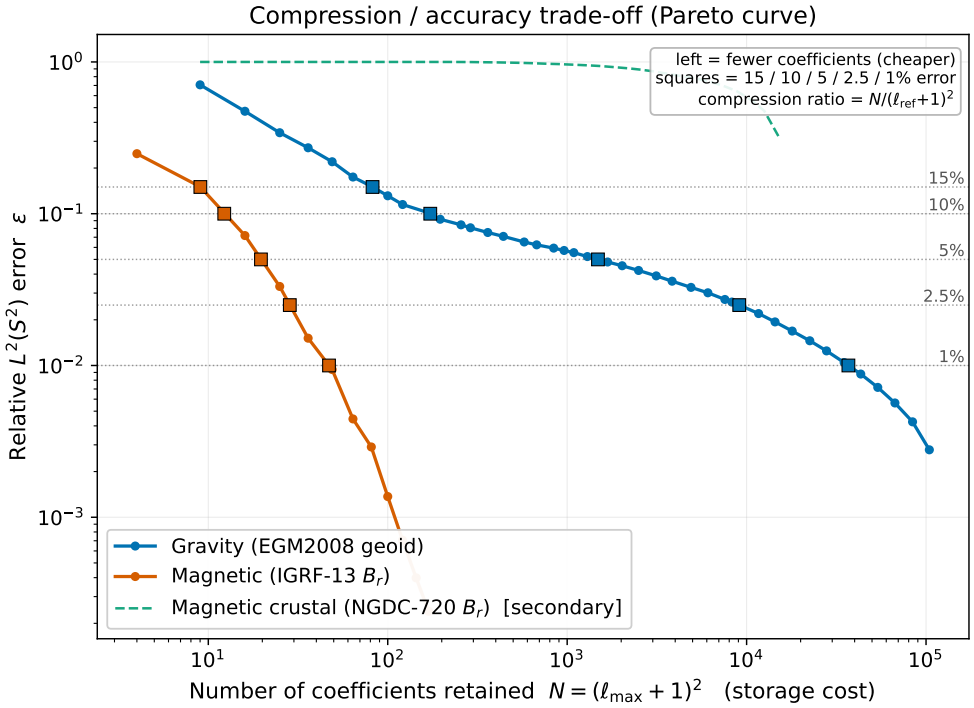

Fig. 5 Relative error ε versus retained coefficient count $N = (\ell_{\max}+1)^2$ (both axes logarithmic). The main-field curve lies below the geoid at every storage budget up to degree 13, while the crustal field (secondary) compresses poorly; the 1 per cent coefficient counts, and the storage ratio between fields, are those of Table 1. Squares mark the 15, 10, 5, 2.5, and 1 per cent levels.

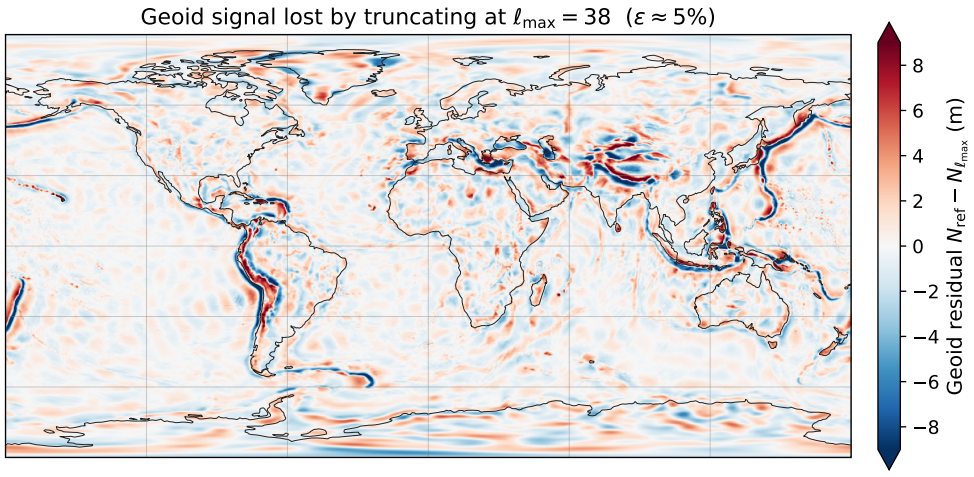

Fig. 6 Geoid signal discarded by truncation: the residual $N_{\mathrm{ref}} - N_{\ell_{\max}}$ (metres) between the reference geoid ($\ell_{\mathrm{ref}} = 360$) and its truncation at $\ell_{\max} = 38$ (where ε is about 5 per cent). Diverging colour scale centred at zero.

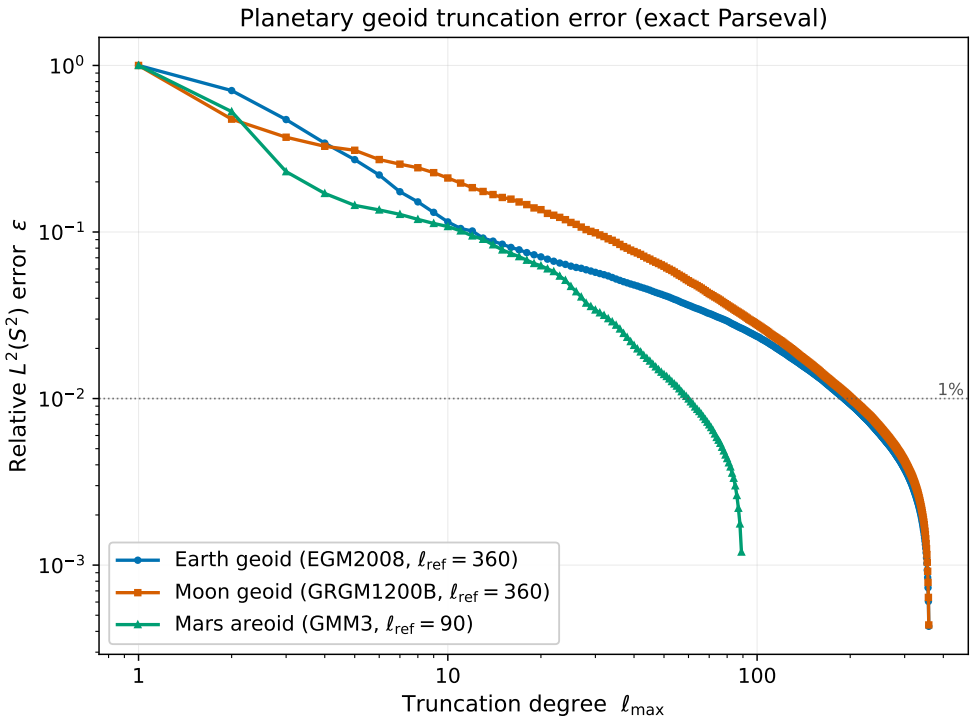

Fig. 7 Exact relative $L^2(S^2)$ truncation error $\varepsilon(\ell_{\max}) = \left(\sum_{\ell>\ell_{\max}} \sigma_\ell^2 / \sum_\ell \sigma_\ell^2\right)^{1/2}$ for the geoids of Earth (EGM2008), the Moon (GRGM1200B (Goossens et al. 2020)) and Mars (GMM3 (Genova et al. 2016)) on log–log axes; the dotted line marks the 1 per cent level. Earth and the Moon are both referenced to $\ell_{\mathrm{ref}} = 360$ and are directly comparable. Mars uses a lower-degree model referenced to $\ell_{\mathrm{ref}} = 90$ and is therefore *not* comparable on coefficient count with Earth or the Moon. Values from `planetary_curves.csv`. The decay slope and the degree at a fixed error tolerance are distinct summaries: the slope is a local rate of decay, the 1 per cent crossing a level-dependent threshold, and the two need not move together—the Moon decays with a steeper slope than Earth yet crosses 1 per cent at a higher degree, its normalized error lying above Earth's at every degree from 5 to 359. For the Moon the measured slope -0.961 and the asymptotic prediction $(1-\alpha)/2 = -1.150$ differ by more than for Earth (-0.861 versus -0.919; Table 2): the finite-window slope is a tail-weighted average, and the discrepancy grows with the spectrum's curvature away from a pure power law, the Moon's spectrum being more curved than Earth's—the same mechanism as Earth's smaller gap, amplified.

The gravity-functional block exhibits the Meissl order shift of Corollary 2. Along the ladder geoid N ($t = 0$), disturbance δg and anomaly Δg (both first radial derivatives of the disturbing potential, $t = 1$), and radial gradient T_{rr} ($t = 2$), the fitted spectral index steps by $\Delta\hat{\alpha} \approx 2$ per radial-derivative order: $\hat{\alpha} : 2.96 \to 0.98$ across the first derivative, $0.93 \to -0.97$ across the next, while the same-order pair $\delta g, \Delta g$ differs by only 0.05—the prediction $\Delta\alpha = 2t$ to within the $O(\ell^{-1})$ lower-order terms of the $(\ell\pm1)$ weights. Because each functional's degree variance is the exact rescaling $w_\ell^2\sigma_\ell^2(T)$ of the single measured disturbing-potential spectrum, this is a consistency check on those corrections rather than an independent measurement; and since each derivative lowers

the index by two, δg, Δg, and T_{rr} fall below $\alpha = 1$, out of the rate identity (dashed in the table), so only the index-shift branch of the corollary is exercised by these fields.

Table 2 Extended results companion to Table 1: decay exponent $\hat{p}$ (the ε log–log slope), spectral index $\hat{\alpha}$ ($\sigma_\ell^2 \propto \ell^{-\alpha}$), the analytic asymptotic prediction $(1-\hat{\alpha})/2$, and the 1 per cent truncation degree and coefficient count, across planetary geoids (lunar model GRGM1200B (Goossens et al. 2020), Mars model GMM3 (Genova et al. 2016)), gravity functionals, and the temporal main field. The analytic $(1-\hat{\alpha})/2$ matches the measured $\hat{p}$ only for the in-regime ($\alpha > 1$) reddest fields (the planetary geoids and the geoid functional); a dash marks the out-of-regime rows ($\alpha \leq 1$: disturbance, anomaly, gradient), where the asymptotic prediction does not apply, and for the band-limited main field it is an effective index only, as noted for the spectral fit in Methods. Values from `planetary.csv`, `functionals.csv` and `temporal_igrf.csv`; the planetary geoid error curves are plotted in Figure 7. The Earth geoid row ($\hat{p} = -0.861$) uses the pyshtools round-trip path (Bruns correction with latitude-dependent γ) and the Geoid N functional row ($\hat{p} = -0.898$) the raw-Stokes path (fixed mean γ); the 4 per cent difference reflects the latitude dependence of $\gamma(\varphi)$ in the first-order Bruns correction. Each temporal main-field row is measured against that epoch's effective reference degree—the last non-zero IGRF degree, $\ell_{\mathrm{ref}} = 10$ for 1900 (IGRF carries no degrees 11–13 before 2000; fit window $\ell = 1$–9) and $\ell_{\mathrm{ref}} = 13$ for 2020 (window $\ell = 1$–12)—so no epoch is zero-padded to a common band. Coefficient counts use the unrounded 1 per cent degree; the disturbance value $\ell_{1\%} = 357.03$ (displayed rounded) thus rounds up to degree 358, giving $359^2 = 128{,}881$.

Field	$\hat{p}$	$\hat{\alpha}$	$(1-\hat{\alpha})/2$	ε=1%	Coeffs at 1%
Planetary geoids					
Earth (EGM2008)	−0.861	2.839	−0.919	191.2	37,249
Moon (GRGM1200B)	−0.961	3.300	−1.150	201.7	41,209
Mars (GMM3)	−1.129	3.448	−1.224	59.8	3,721
Gravity functionals (Earth, raw-Stokes path)					
Geoid N	−0.898	2.959	−0.979	194.9	38,416
Disturbance δg	−0.253	0.982	—	357.0	128,881
Anomaly Δg	−0.241	0.934	—	357.5	128,881
Gradient T_{rr}	−0.076	−0.972	—	359.0	129,600
Temporal main field (IGRF-13)					
Epoch 1900	−2.370	6.066	−2.533	5.6	49
Epoch 2020	−2.924	7.509	−3.254	5.9	49

Verification. The grid-based error and the analytic Parseval prediction of (1) agree to better than 2×10^{-14} in relative terms for every field. The Gauss–Legendre weights integrate the sphere to 4π with an error of about 9×10^{-15}. For the magnetic main field the degree variance recomputed directly from the raw Gauss coefficients matches the gridded field to a relative difference below 10^{-12}. The independent equiangular $\sin\theta$ quadrature reproduces the Gauss–Legendre error to 4×10^{-7}, whereas the deliberately unweighted average differs by 0.07 in ε, confirming that the area weighting is both correct and necessary (these cross-checks are recorded in `results/verification.json`). The error curve is monotonically non-increasing for every field, and the threshold degrees are correctly ordered. As a sensitivity note, the geoid 1 per cent threshold

depends on the treatment of the degree-2 term: with the standard ellipsoid-referenced geoid it lies near degree 191, and excluding degree 2 entirely raises it to about 219, while the decay slope is essentially unchanged.

5 Discussion

Findings and interpretation. Across the two primary fields the truncation behaviour differs markedly, and the difference tracks the physical source depth. The geoid loses accuracy slowly, needing of order 10^4 coefficients to reach 1 per cent, whereas the radial main field reaches the same accuracy with a few tens; the secondary crustal field decays more slowly than either. These differences follow directly from the degree-variance spectra (Figure 3) through (1)—a steep spectrum yields a fast-falling error, a shallow one a slow-falling error—and the spectral shape in turn reflects where each field is generated. The geomagnetic main field originates in the fluid outer core and is dominated by the degree-1 dipole (Backus et al. 1996; Finlay et al. 2016), so its power concentrates at the lowest degrees and it is the most compressible; the geoid reflects density structure distributed through crust and mantle and carries appreciable power across many degrees (Kaula 1963; Rapp 1989), so it is intermediate; the crustal magnetic field, from shallow laterally varying magnetisation, is nearly white (Maus 2008, 2010) and least compressible. Consequently "the magnetic field compresses better than gravity" holds only for the core/main field: the crustal magnetic field compresses worse than gravity, so magnetism is not a single category in this respect.

Physical scales. To connect truncation degree to familiar spatial scales, the geoid's 5 per cent threshold near degree 38 corresponds to a harmonic half-wavelength $\lambda/2 = \pi R/38 \approx 527$ km, whereas the deep, dipole-dominated main field reaches 1 per cent already by degree 6, consistent with the compressibility ranking in which the deepest source produces the longest-wavelength, most compressible signal and the shallowest the least compressible one.

Compressibility with source depth. Figure 8 reports the 1 per cent truncation degree and the decay slope of the IGRF-13 main field as it is analytically continued from Earth's surface to the core–mantle boundary (CMB). Downward continuation multiplies each degree-ℓ radial-field coefficient by $(a/r)^{\ell+2}$ (the potential factor $(a/r)^{\ell+1}$ times one further power for the radial derivative), so the higher degrees are amplified progressively more as the evaluation radius r decreases from the surface toward the CMB. This flattens the degree-variance spectrum, moving relative power to higher degrees and raising the degree at which the 1 per cent error is reached (from 5.9 at the surface to 13.0 at the CMB) while the decay slope shallows. Two caveats, one on the Sobolev index, one on the model's noise floor, govern the reading of this trend and are collected after Proposition 2.

The flattening in Figure 8 recovers a classical geomagnetic inference. Continued to the core–mantle boundary the main-field spectrum becomes approximately white, and a near-white spectrum at the core radius is the observation on which the classical

spectral estimate of the core radius rests—the geomagnetic power spectrum, extrapolated inward, is flattest at the source depth (Lowes 1974; Langel and Estes 1982). The compressibility framework reaches the same statement through its own quantity: the ε-decay slope shallows monotonically from -2.92 at the surface toward -0.43 at the CMB, the storage-side signature of a whitening spectrum. This continues the degree-13 model rather than measuring the field at depth—the caveats above stand—but within that scope the compressibility slope reproduces the white-core result.

Proposition 2 (Spectral transform under continuation)**.** *Continuation through a source-free (harmonic) shell to radius r scales the degree-ℓ radial-field coefficient by $(a/r)^{\ell+2}$ and hence the degree variance by $\sigma_\ell^2(r) = (a/r)^{2\ell+4}\,\sigma_\ell^2(a)$; the degree-independent factor $(a/r)^4$ cancels in the normalised error ε, leaving the per-degree reweighting $(a/r)^{2\ell}$. For a power-law surface spectrum this reweighting is exponential in ℓ, so the algebraic Sobolev index is the wrong invariant—the* asymptotic *index saturates ($s_* = +\infty$ for $r > a$, undefined for $r < a$)—while the clean, closed-form relationship lives in the analyticity rate $\tau(r) = \ln(r/a)$.*

Proof The reweighting

$$(a/r)^{2\ell} = e^{-2\ell \ln(r/a)}$$

is exponential in ℓ, whereas the Sobolev weight $(1+\ell(\ell+1))^s \sim \ell^{2s}$ is algebraic, so no finite s tracks it and the smoothness scale that does is the analytic one.

For $r > a$ (upward, $\ln(r/a) > 0$) set $\beta = 2\ln(r/a) > 0$, so that $\sigma_\ell^2(r) = (a/r)^4\, e^{-\beta\ell}\, \sigma_\ell^2(a)$. For a power-law surface spectrum $\sigma_\ell^2(a) \sim C\ell^{-\alpha}$ and any fixed exponent $k > 0$,

$$\ell^k \sigma_\ell^2(r) \sim C(a/r)^4\, \ell^{\,k-\alpha}\, e^{-\beta\ell} \longrightarrow 0 \qquad (\ell \to \infty),$$

since the exponential $e^{-\beta\ell}$ overwhelms the power $\ell^{\,k-\alpha}$ for every k; the coefficients therefore decay faster than any power of ℓ. Consequently $\sum_\ell (1+\ell(\ell+1))^s \sigma_\ell^2(r) < \infty$ for *all* s, so the continued field lies in H^s for every s ($s_* = +\infty$) and is thus C^∞. Super-algebraic decay alone yields only C^∞; real-analyticity requires the stronger *geometric* decay, which continuation supplies: with $\tau = \frac{1}{2}\beta = \ln(r/a) > 0$ the coefficients satisfy $|c_{\ell m}(r)| = O(e^{-\tau\ell})$, so the solid-harmonic extension $\sum_{\ell,m} (a/\rho)^{\ell+1}\,[\,\cdot\,]\,Y_{\ell m}$ converges throughout the open source-free shell $\rho > a$. The evaluation sphere $\rho = r$ lies strictly interior to that shell (harmonic on both sides), so the continued field is the restriction of a function harmonic—hence real-analytic—on an open neighbourhood of the sphere, and is therefore real-analytic on S^2, with analyticity rate $\tau = \ln(r/a)$.

For $r < a$ (downward) the sign reverses: with $\gamma = 2\ln(a/r) > 0$,

$$\sigma_\ell^2(r) = (a/r)^4\, e^{\gamma\ell}\, \sigma_\ell^2(a) \sim C(a/r)^4\, \ell^{-\alpha}\, e^{\gamma\ell} \longrightarrow \infty,$$

so the summands of $\sum_\ell \sigma_\ell^2(r)$ do not even tend to zero—the ratio of successive terms tends to $e^\gamma > 1$—and the series diverges by the term test (equivalently the ratio test). The limit has infinite L^2 norm and lies in no H^s; this is the classical ill-posedness of downward continuation, established in the constructive-approximation setting by Freeden et al. (Freeden et al. 1998). In neither direction is s_* informative: the continuation shifts τ, not s_*. □

Two caveats govern how Figure 8 should be read, and are collected here. First, on the Sobolev index: $s_* = +\infty$ refers to the idealised infinite-band power law, whereas the degree-13 field actually computed is a trigonometric polynomial, hence C^∞ at

every radius, so no Sobolev index is assigned to it; the plotted $\ell_{1\%}$ and finite-window slope nevertheless remain *valid finite-band compressibility descriptors* of the continued model field—the coefficient count to reach 1 per cent error at radius r is a real, well-defined property, and the reddening is a genuine spectral re-weighting. What continuation severs is only the reading of that slope as a smoothness index, since the surface field's slope–s_* correspondence does not survive. Second, on the noise floor: the continuation acts on the degree-13 IGRF coefficients, whose highest degrees already lie near the model's noise floor, so the trend characterises the model field rather than a measurement of the field at depth—in the finite band the idealised ill-posedness appears not as divergence but as amplification of those top, near-noise-floor degrees, the practical face of the operator's unboundedness.

Corollary 2 and Proposition 2 are two ends of one operator family. A finite-order Meissl transfer (symbol $\lambda_\ell \sim \ell^t$) moves the Sobolev index s_* by $-t$ along the algebraic scale; radial continuation reweights each degree by a factor exponential in ℓ, $e^{\pm\tau\ell}$ with $\tau = \ln(r/a)$, a symbol asymptotic to no power ℓ^t, so it does not move s_*—which saturates to $\pm\infty$—but the analyticity rate τ. The pair (s_*, τ) therefore classifies a geopotential functional under this family: the finite-order transfer sets its algebraic (Sobolev) compressibility rate, radial continuation its exponential (analytic) one.

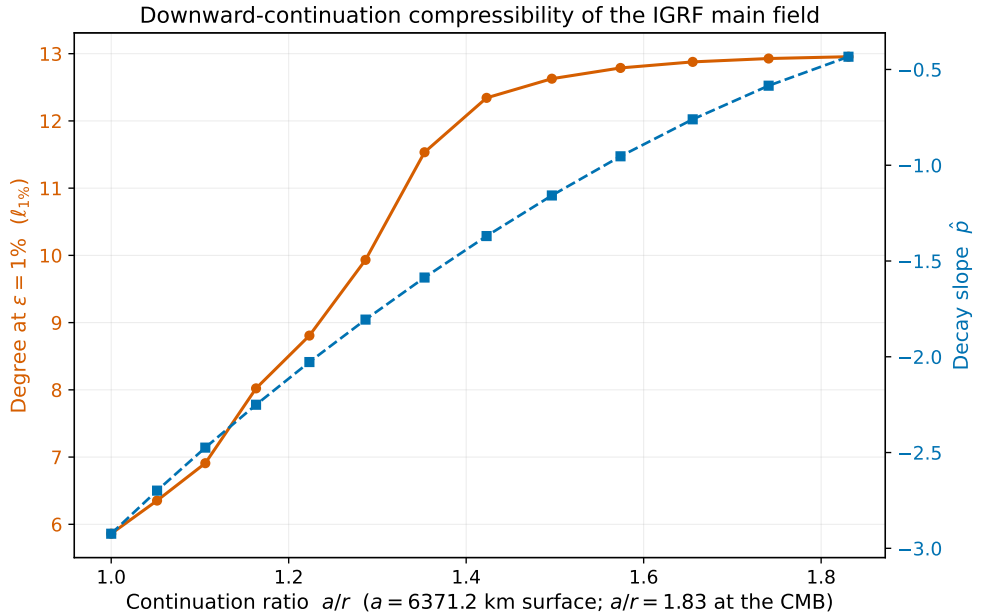

Fig. 8 Compressibility of the IGRF-13 radial main field under analytic downward continuation from Earth's surface ($a/r = 1$) to the core–mantle boundary ($a/r \approx 1.83$, $r \approx 3480$ km). Left axis (circles): the degree $\ell_{1\%}$ at which the relative error reaches 1 per cent, rising from 5.9 at the surface to 13.0 at the CMB. Right axis (squares): the log–log decay slope $\hat{p}$, changing from -2.92 to -0.43. Values from `radius_compressibility.csv`. This is the analytic continuation of the degree-13 IGRF model; see the caveats following Proposition 2.

Fairness of the comparison. Each field's error is measured against its own reference degree, so the absolute curves have different horizontal extents; the scale-free comparator is the log–log slope, which is independent of that choice. The geoid is the "reddest" (most low-degree-dominated) of the common gravity functionals, so it is the most favourable case for gravity—and even so it is less compressible than the core field.

Compression efficiency. Degree truncation incurs two separable kinds of inefficiency. The first is *coefficient* inefficiency: could a reordering of basis functions store fewer coefficients at matched error? By the Kolmogorov n-width of the isotropic Sobolev class $B^{s_*}(S^2)$, degree truncation is rate-optimal among all n-dimensional linear approximations (Pinkus 1985; Kamzolov 1982); coefficient efficiency $\eta_{\mathrm{coeff}} = 1$ in the order sense. This is confirmed empirically: an oracle best-N-term selection (keeping the N largest coefficients) lowers the geoid 1 per cent error by only 0.3 percentage points relative to degree truncation (Table 1)—and since the best-N-term equivalence assumes equal power within each degree, that 0.3-point residual is itself a direct measurement of the within-degree, order-m power inhomogeneity of the real coefficients. Localised bases such as wavelets or Slepian functions can improve on this only for *regionally concentrated* signals; for the globally distributed fields here no significant coefficient gain is available. These notions form a hierarchy of increasing adaptivity: the Kolmogorov n-width fixes one n-dimensional subspace in advance; best-N-term selection adapts the retained set to each field within a fixed basis (the diagonal Eckart–Young case above); and dictionary or best-basis methods adapt the basis itself. For an isotropic Sobolev class—an L^2-based smoothness ball—the first two share the rate $n^{-s_*/2}$ (a coincidence special to L^2-based smoothness; for Besov classes of lower integrability, nonlinear approximation strictly improves the rate (DeVore 1998)), so adaptivity *within* the harmonic basis changes only the constant, as the 0.3-percentage-point best-N-term gap confirms; the payoff of the most adaptive, basis-learning methods is thus confined to signals that break global isotropy or to ill-posed inverse recovery. A complementary line of geomathematical work indeed *learns* a best basis or dictionary for gravitational field modelling—pruning an overcomplete dictionary of spherical harmonics and radial basis functions by regularized functional matching pursuit (Michel and Schneider 2020), more recently combining local and global trial functions at satellite resolution (Schneider and Michel 2024)—but does so to stabilise the ill-posed downward-continuation *inverse* problem, whereas the coefficient-optimality considered here concerns the well-posed *forward* problem of storing an already-estimated coefficient set.

The second is *bit* inefficiency. Storing each retained coefficient as a 32-bit float uses more bits than the coefficient statistics require. Modelling the coefficients as independent Gaussian sources with per-coefficient variance $\sigma^2_{\ell m} = \sigma^2_\ell/(2\ell+1)$, the reverse water-fill construction (Cover and Thomas 2006) gives the bit rate B_{WF} at the target distortion $D = \varepsilon^2\|f\|^2$.

The independence assumption is worth examining, since geophysical coefficients are cross-degree correlated. Coding each coefficient with its own marginal quantizer is a feasible scheme attaining rate B_{WF} at distortion D, so the true correlated-Gaussian optimum can only be smaller, $R_\Sigma(D) \le B_{\mathrm{WF}}$ at every D (derived explicitly below).

The independent-Gaussian rate B_{WF} is therefore an *upper* bound on the genuine rate–distortion floor, not a barrier a real coder cannot cross. Two distinct routes lie below it: a joint (vector) code can exploit cross-degree correlation, and—independently of any correlation—the quantized-symbol marginals can themselves be more compressible than the Gaussian bound. The entropy coder in Figure 9 is a *scalar*, correlation-blind coder, so its dip beneath the independent-Gaussian curve is the second route: the quantized symbols carry less than the Gaussian bound, confirming that the independent-source floor overstates the true one. Measured on the real coefficient sets at 1 per cent error, the entropy of the quantized symbols is 0.67 and 0.94 times B_{WF} for the main field and crustal field—below unity, a direct signature of non-Gaussian (peaked) coefficient marginals—whereas for the geoid it is 1.23 times B_{WF}, the scalar quantiser's overhead there outweighing the marginal non-Gaussianity (`codec_gap.json`). The float32 comparison is only strengthened: because the true floor lies at or below B_{WF}, float32 storage sits *at least* 11.3 times above it. At 1 per cent error, float32 storage of the geoid coefficients uses about 11.3 times more bits than B_{WF}; a water-fill-guided quantizer narrows this to a factor of 1.59 with a simple greedy quantizer and 1.23 with entropy coding of the quantized symbols (Figure 9).

Why the independent-Gaussian rate is an upper bound. The inequality $R_\Sigma(D) \le B_{\mathrm{WF}}$ can be made explicit in the high-rate regime, where every mode is retained. For a zero-mean Gaussian vector of covariance Σ of order n, reverse water-filling at small distortion D equalises the per-mode distortion at D/n, so the optimal rate water-fills the *eigenvalues* λ_i of Σ:

$$R_\Sigma(D) = \sum_{i=1}^{n} \frac{1}{2} \log_2 \frac{\lambda_i}{D/n} = \frac{n}{2} \log_2 \frac{n}{D} + \frac{1}{2} \log_2 \det \Sigma,$$

using $\prod_i \lambda_i = \det \Sigma$. Coding each coefficient with its own marginal quantiser instead water-fills on the *diagonal* entries $\Sigma_{ii} = \sigma^2_{\ell m}$, a feasible scheme of rate

$$B_{\mathrm{WF}}(D) = \sum_{i=1}^{n} \frac{1}{2} \log_2 \frac{\Sigma_{ii}}{D/n} = \frac{n}{2} \log_2 \frac{n}{D} + \frac{1}{2} \log_2 \prod_i \Sigma_{ii}.$$

Subtracting isolates the gap exactly at Hadamard's inequality,

$$B_{\mathrm{WF}}(D) - R_\Sigma(D) = \frac{1}{2} \log_2 \frac{\prod_i \Sigma_{ii}}{\det \Sigma} \;\ge\; 0,$$

which is non-negative because $\det \Sigma \le \prod_i \Sigma_{ii}$ for every positive-definite Σ, with equality iff Σ is diagonal, i.e. the coefficients are uncorrelated. Hence $R_\Sigma(D) \le B_{\mathrm{WF}}(D)$, and the independent-source rate overstates the true floor by the log-ratio of the arithmetic to the geometric spread of the eigenvalues. These closed forms are the high-rate illustration; the inequality itself needs no high-rate assumption, since marginal coding is a feasible scheme achieving $B_{\mathrm{WF}}(D)$ at every D, so the correlated optimum can only be smaller, and the high-rate identity fixes the gap at the Hadamard log-ratio. Because the Gaussian is the least compressible source of a given covariance under

mean-squared error (Cover and Thomas 2006), the bound holds a fortiori against the true, possibly non-Gaussian coefficients.

Bit efficiency therefore depends on the codec, not on the choice of truncation degree, and improving it is fully compatible with the coefficient-optimal degree-truncation strategy.

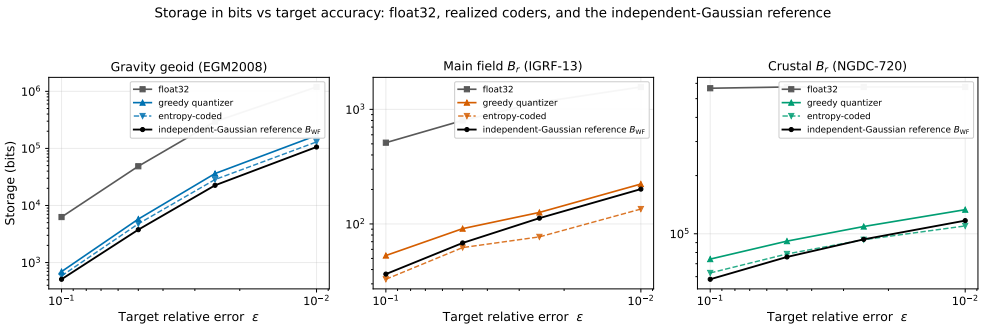

Fig. 9 Storage in bits versus target relative error ε (both axes logarithmic; accuracy increases left to right) for the geoid, radial main field, and crustal field. Each panel shows float32 coefficient storage, the independent-Gaussian rate–distortion reference B_{WF} (reverse water-filling of independent Gaussian coefficients; a floor only under that model), and two realized coders: a greedy scalar quantizer (B_{real}) and entropy coding of the quantized symbols (B_{entropy}). Values from `codec_gap.json` and `water_fill.json`. For the geoid at $\varepsilon = 1$ per cent, float32 is 11.3 times B_{WF}, the greedy coder 1.59 times and the entropy coder 1.23 times; per-field values at the four error levels are plotted. Entropy values below 1 indicate the quantized-symbol entropy falls under the independent-Gaussian reference: the entropy coder is scalar and correlation-blind, so this dip reflects non-Gaussian (peaked) coefficient marginals rather than cross-degree correlation (see the bit-inefficiency discussion). float32 sits far above B_{WF} because a fixed 32-bit representation spends the same precision on every coefficient, whereas the coefficient magnitudes span many orders of magnitude; the residual greedy- and entropy-coded gaps reflect the limits of scalar quantisation.

Global scope and localised alternatives. The truncation studied here is a global operation: a single $\ell_{\max}$ applies uniformly over the sphere. Slepian functions (Simons et al. 2006) concentrate bandlimited signal within a chosen region and are the L^2-optimal localisation of a global spherical-harmonic basis. Constructive approximation on the sphere offers a wider family of such localised systems—spherical splines and wavelets (Freeden et al. 1998), and greedy multiscale dictionaries combining spherical harmonics with scaling functions and wavelets (Michel and Telschow 2014)—which likewise pay off only for spatially concentrated or multiscale-structured signals. For the globally distributed fields analysed here, the Slepian and truncation representations converge (in the limit of a full-sphere region they are identical), so no compression gain arises from spatially concentrated bases. A regionally focused analysis—for example, the geoid anomaly of a single tectonic plate—could in principle reduce the coefficient count by roughly the reciprocal of the fractional area covered, but requires a distinct error metric and is outside the present global scope. A supplementary comparison against a biorthogonal bior4.4 wavelet (`results/wavelet_comparison.json`) makes this concrete on a local geoid patch—the setting most favourable to a localised basis:

reaching 5 and 1 per cent error there takes 665 and 2180 nonzero wavelet coefficients, and the wavelet's coded size still exceeds the spherical-harmonic representation of the same patch by factors of 1.4 and 1.9 (its per-coefficient index overhead outweighs its sparsity), so degree truncation retains the advantage even locally, let alone globally.

Limitations. Several choices bound the results. The reference degrees (360 for the geoid, 13 for the main field, 133 for the crustal field) define what counts as the full signal; a different reference would shift the absolute thresholds, though not the qualitative ordering. The geoid was synthesised with first-order Bruns, which omits a second-order term of order $N^2/R \sim 1$ mm for the largest undulations ($N \lesssim 100$ m, $R \approx 6371$ km) and is therefore negligible at the metre scale analysed here. Its low-degree (especially degree-2) power depends on the reference-ellipsoid and tide-system conventions, which is the origin of the modest sensitivity of the 1 per cent threshold noted above. The crustal model is itself truncated to degree 133 from a higher-degree model, so its threshold degrees lie close to its reference and are best read through its decay slope. The compression ratio counts coefficients only and does not model quantisation or entropy coding, so it is an upper bound on what a real codec would store. The rate-distortion and codec results of Section 5 give the bit-level picture. The effective information ceiling of EGM2008 at degree 1787 (where the per-degree SNR drops to unity; see Introduction) is distinct from the compression threshold: the geoid 1 per cent accuracy threshold is at degree 191, well within the signal-dominated band, so model noise does not affect the compression results reported here.

6 Conclusion

This study characterised, on a common area-weighted footing, how the reconstruction error of Earth's geoid and radial magnetic field decreases with spherical-harmonic truncation degree. The geoid error decays with a log–log slope near -0.861 and reaches 1 per cent only near degree 191.2, about 37,249 coefficients, whereas the radial main field decays with slope near -2.924 and reaches 1 per cent near degree 5.9, about 49 coefficients; a crustal magnetic model decays more slowly than either. The grid-based error agrees with the analytic Parseval prediction to better than 10^{-13} and with an independent recomputation from the raw coefficients, and the area weighting was verified explicitly.

Beneath these numbers is a single organising exponent. For each field in the asymptotic, red-spectrum ($\alpha > 1$) regime the measured error-decay slope, the Sobolev smoothness index, and the Kolmogorov n-width rate are one and the same quantity—the power-law specialisation of the classical link between approximation rate and smoothness, here measured field by field and its regime mapped—so the compressibility of a potential field is an approximation-theoretic descriptor of its spectral character, which in turn tracks its source depth: the deep, dipole-dominated core field is the most compressible and the shallow, near-white crustal field—characterised by its decay slope alone, outside the three-way identity—the least. Within this picture spherical-harmonic truncation is coefficient-optimal in the rate (order) sense for the globally isotropic fields considered, which locates the remaining, purely bit-level, inefficiency in the storage format rather than the basis. Future work could extend the comparison

to additional derived functionals, to higher reference degrees, and to alternative basis choices, while retaining the same verified, area-weighted error metric.

A Spherical-harmonic resolution

Table 3 relates the truncation degree to the spatial half-wavelength it resolves, $\lambda/2 = \pi R/\ell_{\max}$ with $R \approx 6371$ km, and to the coefficient count $(\ell_{\max}+1)^2$. Degree 2190, the EGM2008 maximum, corresponds to a ∼9 km harmonic half-wavelength and 4,800,481 coefficients—the finer scales sometimes quoted for such models come from auxiliary topographic data, not the harmonic truncation. (Values computed by `resolution.py`; see `results/resolution.csv`.)

Table 3 Spherical-harmonic resolution: half-wavelength $\lambda/2 = \pi R/\ell_{\max}$ ($R \approx 6371$ km) and coefficient count $(\ell_{\max}+1)^2$ versus truncation degree.

Degree $\ell_{\max}$	$\lambda/2$ (km)	Coefficients
10	2002	121
13	1540	196
36	556	1,369
90	222	8,281
180	111	32,761
360	55.6	130,321
720	27.8	519,841
1080	18.5	1,168,561
2190	9.1	4,800,481

Declaration of competing interest

The authors declare that they have no known competing financial interests or personal relationships that could have appeared to influence the work reported in this paper.

Funding

This research did not receive any specific grant from funding agencies in the public, commercial, or not-for-profit sectors.

Data and Code Availability

The analysis code and all derived results are openly available at https://github.com/pa1aash/spherical-harmonics-earth-fields-data-release (on Zenodo at https://doi.org/10.5281/zenodo.20716351). A single pipeline command (`make all`) reproduces all figures and tables from model downloads, and the numerical routines are validated by an accompanying test suite of 139 tests (`make test`).

Acknowledgments

The authors thank the developers of `pyshtools`, `boule`, NumPy, SciPy and Matplotlib for the open-source tools used in this work, and the providers of the EGM2008, IGRF-13 and NGDC-720 models for public access to the data.

References

Alken P, Thébault E, Beggan CD, et al (2021) International Geomagnetic Reference Field: the thirteenth generation. Earth, Planets and Space 73(1):49. https://doi.org/10.1186/s40623-020-01288-x

Atkinson K, Han W (2012) Spherical Harmonics and Approximations on the Unit Sphere: An Introduction, Lecture Notes in Mathematics, vol 2044. Springer, Berlin, Heidelberg, https://doi.org/10.1007/978-3-642-25983-8

Backus G, Parker R, Constable C (1996) Foundations of Geomagnetism. Cambridge University Press, Cambridge

Chang G, Bian S (2023) Least-squares collocation: a spherical harmonic representer theorem. Geophysical Journal International 234(2):879–886. https://doi.org/10.1093/gji/ggad075

Cover TM, Thomas JA (2006) Elements of Information Theory, 2nd edn. Wiley-Interscience, Hoboken, New Jersey, https://doi.org/10.1002/047174882X

Dai F, Xu Y (2013) Approximation Theory and Harmonic Analysis on Spheres and Balls. Springer Monographs in Mathematics, Springer, New York, https://doi.org/10.1007/978-1-4614-6660-4

DeVore RA (1998) Nonlinear approximation. Acta Numerica 7:51–150. https://doi.org/10.1017/S0962492900002816

DeVore RA, Lorentz GG (1993) Constructive Approximation, Grundlehren der mathematischen Wissenschaften, vol 303. Springer-Verlag, Berlin, https://doi.org/10.1007/978-3-662-02888-9

Driscoll JR, Healy DM (1994) Computing Fourier transforms and convolutions on the 2-sphere. Advances in Applied Mathematics 15(2):202–250. https://doi.org/10.1006/aama.1994.1008

Eckart C, Young G (1936) The approximation of one matrix by another of lower rank. Psychometrika 1(3):211–218. https://doi.org/10.1007/BF02288367

Finlay CC, Olsen N, Kotsiaros S, et al (2016) Recent geomagnetic secular variation from Swarm and ground observatories as estimated in the CHAOS-6 geomagnetic field model. Earth, Planets and Space 68:112. https://doi.org/10.1186/

s40623-016-0486-1

Freeden W, Gervens T, Schreiner M (1998) Constructive Approximation on the Sphere: With Applications to Geomathematics. Numerical Mathematics and Scientific Computation, Clarendon Press, Oxford University Press, Oxford

Genova A, Goossens S, Lemoine FG, et al (2016) Seasonal and static gravity field of Mars from MGS, Mars Odyssey and MRO radio science. Icarus 272:228–245. https://doi.org/10.1016/j.icarus.2016.02.050

Goossens S, Sabaka TJ, Wieczorek MA, et al (2020) High-resolution gravity field models from GRAIL data and implications for models of the density structure of the Moon's crust. Journal of Geophysical Research: Planets 125(2):e2019JE006086. https://doi.org/10.1029/2019JE006086

Harris CR, Millman KJ, van der Walt SJ, et al (2020) Array programming with NumPy. Nature 585(7825):357–362. https://doi.org/10.1038/s41586-020-2649-2

Hirt C, Claessens S, Fecher T, et al (2013) New ultrahigh-resolution picture of Earth's gravity field. Geophysical Research Letters 40(16):4279–4283. https://doi.org/10.1002/grl.50838

Holmes SA, Featherstone WE (2002) A unified approach to the Clenshaw summation and the recursive computation of very high degree and order normalised associated Legendre functions. Journal of Geodesy 76(5):279–299. https://doi.org/10.1007/s00190-002-0216-2

Hunter JD (2007) Matplotlib: A 2D graphics environment. Computing in Science & Engineering 9(3):90–95. https://doi.org/10.1109/MCSE.2007.55

Kamzolov AI (1982) The best approximation of classes of functions $w_p^\alpha(s^n)$ by polynomials in spherical harmonics. Mathematical Notes of the Academy of Sciences of the USSR 32(3):622–628. https://doi.org/10.1007/BF01140192, translated from Matematicheskie Zametki 32(3):285–293

Kaula WM (1963) Elastic models of the mantle corresponding to variations in the external gravity field. Journal of Geophysical Research 68(17):4967–4978. https://doi.org/10.1029/JZ068i017p04967

Kaula WM (1966) Theory of Satellite Geodesy: Applications of Satellites to Geodesy. Blaisdell Publishing Company, Waltham, Massachusetts

Langel RA, Estes RH (1982) A geomagnetic field spectrum. Geophysical Research Letters 9(4):250–253. https://doi.org/10.1029/GL009i004p00250

Lowes FJ (1966) Mean-square values on sphere of spherical harmonic vector fields. Journal of Geophysical Research 71(8):2179. https://doi.org/10.1029/

JZ071i008p02179

Lowes FJ (1974) Spatial power spectrum of the main geomagnetic field, and extrapolation to the core. Geophysical Journal of the Royal Astronomical Society 36(3):717–730. https://doi.org/10.1111/j.1365-246X.1974.tb00622.x

Mauersberger P (1956) Das Mittel der Energiedichte des geomagnetischen Hauptfeldes an der Erdoberfläche und seine säkulare änderung. Gerlands Beiträge zur Geophysik 65:207–215

Maus S (2008) The geomagnetic power spectrum. Geophysical Journal International 174(1):135–142. https://doi.org/10.1111/j.1365-246X.2008.03820.x

Maus S (2010) An ellipsoidal harmonic representation of Earth's lithospheric magnetic field to degree and order 720. Geochemistry, Geophysics, Geosystems 11(6):Q06015. https://doi.org/10.1029/2010GC003026

Michel V, Schneider N (2020) A first approach to learning a best basis for gravitational field modelling. GEM – International Journal on Geomathematics 11(1):9. https://doi.org/10.1007/s13137-020-0143-5

Michel V, Telschow R (2014) A non-linear approximation method on the sphere. GEM – International Journal on Geomathematics 5(2):195–224. https://doi.org/10.1007/s13137-014-0063-3

Mirsky L (1960) Symmetric gauge functions and unitarily invariant norms. The Quarterly Journal of Mathematics 11(1):50–59. https://doi.org/10.1093/qmath/11.1.50

Moritz H (1980) Geodetic Reference System 1980. Bulletin Géodésique 54(3):395–405. https://doi.org/10.1007/BF02521480

Pail R, Bruinsma S, Migliaccio F, et al (2011) First GOCE gravity field models derived by three different approaches. Journal of Geodesy 85(11):819–843. https://doi.org/10.1007/s00190-011-0467-x

Pavlis NK, Holmes SA, Kenyon SC, et al (2012) The development and evaluation of the Earth Gravitational Model 2008 (EGM2008). Journal of Geophysical Research: Solid Earth 117(B4):B04406. https://doi.org/10.1029/2011JB008916

Pinkus A (1985) n-Widths in Approximation Theory, Ergebnisse der Mathematik und ihrer Grenzgebiete (3), vol 7. Springer-Verlag, Berlin, https://doi.org/10.1007/978-3-642-69894-1

Rapp RH (1989) The decay of the spectrum of the gravitational potential and the topography for the Earth. Geophysical Journal International 99(3):449–455. https://doi.org/10.1111/j.1365-246X.1989.tb02031.x

Rummel R, van Gelderen M (1995) Meissl scheme — spectral characteristics of physical geodesy. Manuscripta Geodaetica 20(5):379–385. https://doi.org/10.1007/BF03655471

Schneider N, Michel V (2024) The likelihood of a regularized functional matching pursuit: combining local and global trial functions for gravitational field modelling. GEM – International Journal on Geomathematics 15(1):8. https://doi.org/10.1007/s13137-024-00255-y

Simons FJ, Dahlen FA, Wieczorek MA (2006) Spatiospectral concentration on a sphere. SIAM Review 48(3):504–536. https://doi.org/10.1137/S0036144504445765

Sneeuw N (1994) Global spherical harmonic analysis by least-squares and numerical quadrature methods in historical perspective. Geophysical Journal International 118(3):707–716. https://doi.org/10.1111/j.1365-246X.1994.tb03995.x

Tapley BD, Bettadpur S, Watkins M, et al (2004) The Gravity Recovery and Climate Experiment: Mission overview and early results. Geophysical Research Letters 31(9):L09607. https://doi.org/10.1029/2004GL019920

Uieda L, Soler SR (2020) Boule: Reference ellipsoids for geodesy, geophysics, and coordinate calculations (Python package, version 0.2.0). https://doi.org/10.5281/zenodo.3939204, zenodo software archive

Virtanen P, Gommers R, Oliphant TE, et al (2020) SciPy 1.0: fundamental algorithms for scientific computing in Python. Nature Methods 17(3):261–272. https://doi.org/10.1038/s41592-019-0686-2

Wieczorek MA, Meschede M (2018) SHTools: Tools for working with spherical harmonics. Geochemistry, Geophysics, Geosystems 19(8):2574–2592. https://doi.org/10.1029/2018GC007529

Wong B (2011) Points of view: Color blindness. Nature Methods 8(6):441. https://doi.org/10.1038/nmeth.1618